
Article:
Li, M., Pietrowski, M.J., De Souza, R.A. et al. (5 more authors) (2014) A family of oxide ion conductors based on the ferroelectric perovskite Na0.5Bi0.5TiO3. Nature Materials, 13 (1). 31 - 35. ISSN 1476-1122

https://doi.org/10.1038/NMAT3782

A family of oxide ion conductors based on the ferroelectric perovskite $Na_{1/2}Bi_{1/2}TiO_3$

Ming Li[1], Martha J. Pietrowski[2], Roger A. De Souza[2], Huairuo Zhang[1], Ian M. Reaney[1], Stuart N. Cook[3], John A. Kilner[3,4] and Derek C. Sinclair[1*]

[1]Department of Materials Science and Engineering, University of Sheffield, Sir Robert Hadfield Building, Mappin Street, Sheffield, S1 3JD, United Kingdom.

[2]Institute of Physical Chemistry, RWTH Aachen University and JARA-FIT, D-52056 Aachen, Germany.

[3]Department of Materials, Imperial College London, London, SW7 2AZ, United Kingdom.

[4]International Institute for Carbon-Neutral Energy Research (I2CNER), 744 Motooka Nishi-ku Fukuoka 819-0395, Japan.

* Author to whom correspondence should be addressed.

E-mail: d.c.sinclair@sheffield.ac.uk.

Introductory paragraph

Oxide ion conductors find important technical applications in electrochemical devices such as solid oxide fuel cells (SOFCs), oxygen separation membranes and sensors[1-9]. $Na_{1/2}Bi_{1/2}TiO_3$ (NBT) is a well-known lead-free piezoelectric material; however, it is often reported to possess high leakage conductivity which is problematic for its piezo- and ferroelectric applications[10-15]. Here we report this high leakage to be oxide ion conduction due to Bi-deficiency and oxygen vacancies induced during materials processing. Mg-doping on the Ti-site increases the ionic conductivity to ~ 0.01 S cm^{-1} at 600 ^{o}C, improves the electrolyte stability in reducing atmospheres and lowers the sintering temperature. This study not only demonstrates how to adjust the nominal NBT composition for dielectric-based applications, but also, more importantly, gives NBT-based materials an unexpected role as a completely new family of oxide ion conductors with potential applications in intermediate temperature SOFCs and opens up a new direction to design oxide ion conductors in perovskite oxides.

Interest in ferroelectric $Na_{1/2}Bi_{1/2}TiO_3$ (NBT) has surged recently mainly driven by the necessity to replace $Pb(Zr_{1-x}Ti_x)O_3$-based piezoelectrics with PbO-free materials, and in the development of high temperature, high permittivity ceramic-based capacitors[10-15]. NBT exhibits maximum relative permittivity, ε_r ~ 3000 at ~ 320 ^oC (T_{max}) and possesses a distorted perovskite structure with extensive chemical, cation-displacement and octahedral tilt disorder.[14] The resulting complex nanodomain structure is well known to facilitate high and temperature stable permittivity behaviour which is suitable for the fabrication of high temperature ceramic capacitors in addition to easy phase switching under the application of a large electric field which creates large strains suitable for actuator applications[10-15]. One drawback of NBT for piezoelectric and capacitor applications, however, is its high leakage conductivity[10,11]. The piezoelectric properties and room temperature dc conductivity depend on the nominal starting composition[10,11], the origin of which has not been resolved. Here we report on the surprising and dramatic sensitivity of the ionic and electronic transport properties of NBT on low levels of A-site nonstoichiometry in the nominal starting composition. We demonstrate that the disordered NBT lattice, dominated by 'soft' covalent bonds, also facilitates rapid diffusion of oxygen ions and NBT may also be compositionally tuned by acceptor-doping (eg. Mg) on the Ti-site to develop a new family of oxide ion conductors.

Complex impedance plane, Z*, plots for samples with nominal starting compositions of $Na_{1/2}Bi_{1/2}TiO_3$ (NBT) and $Na_{1/2}Bi_{1/2+x}TiO_{3\pm\delta}$ (x = -0.01 and 0.01, named $NBi_{0.49}T$ and $NBi_{0.51}T$, respectively) at 500 ^oC are shown in Fig. 1a. $NBi_{0.51}T$ exhibits a single arc within the measured frequency range with an associated resistivity of ~ 8 MΩ cm. The extracted ε_r from the capacitance associated with this arc is ~ 1700, Table S2, and is consistent with the high bulk permittivity value for this ferroelectric material (see

Ref.[10,11] and Fig. S4a), indicating this arc is associated with a grain (bulk) response. For NBT and Bi-deficient ($NBi_{0.49}T$) compositions, similar capacitance and ε_r values are obtained from this arc, Table S2, and therefore confirming it to be a bulk response; however, the associated bulk resistivity, R_b decreases by ~ 3-4 orders of magnitude to ~ 1-2 kΩ cm, inset in Fig. 1a.

An Arrhenius plot of the temperature dependence of the bulk conductivity, σ, where $\sigma = 1/R_b$, Fig. 1b, shows the samples can be divided into two groups. $NBi_{0.51}T$ is insulating with an activation energy, E_a, for bulk conduction of ~ 1.66 eV whereas NBT and $NBi_{0.49}T$ are conducting with E_a ~ 0.8-0.9 eV and ~ 0.4-0.5 eV for the temperature ranges below and above the temperature associated with the maximum in ε_r (T_{max} ~ 320 ^oC) observed in dielectric spectroscopy measurements (see Ref.[10,11] and Fig. S4), respectively.

Two compositions, one conducting (NBT) and the other insulating ($NBi_{0.51}T$), were chosen for further low frequency (down to 1 mHz) Impedance Spectroscopy (IS) measurements. The Z* plots for NBT at 600 ^oC under different atmospheres are shown in Fig. 2. The low frequency (below 10 Hz) data consist of a spike, followed by a slightly distorted semicircle that is strongly dependent on the oxygen partial pressure (pO_2), Fig. 2a. The high frequency arc, inset in Fig. 2b, is associated with the bulk response and is independent of pO_2. The behaviour of the low and high frequency data are consistent with Warburg diffusion and oxygen ionic conduction. Electromotive Force (EMF) measurements using air/nitrogen gas confirm the presence of oxide ion conduction in NBT with an ionic transport number, t_i, > 0.9 at 600-700 ^oC and reducing to ~ 0.84 at 800 ^oC, Fig. 2d. The dependence of low frequency Impedance data associated with the Warburg diffusion on pO_2 and EMF

measurements also suggest that any contribution of Na^+ ion conduction to the ionic conductivity, if any, is small. The intermediate frequency (~ 100 Hz - 100 kHz) arc, Fig. 2b, has an associated capacitance of ~ 4-6 nF cm^{-1} and is assigned as a grain boundary (R_{gb},C_{gb}) response.

For insulating $NBi_{0.51}T$ at 700 ^oC the Z* plot consists primarily of a large arc associated with the bulk response. The dependence of R_b on pO_2 suggests predominantly n-type electronic conduction with E_a ~ 1.66 eV, Fig. 1b. Based on the reported optical band gap, E_g, of ~ 3.3 eV for NBT[15], the electrical conduction in $NBi_{0.51}T$ is close to/dominated by intrinsic electronic conduction where $E_g \sim 2E_a$. Low frequency data indicate ionic conduction is still present but its contribution to the conductivity is much lower. EMF measurements show t_i ~ 0.1 at 600 to 800 ^oC, Fig. 2d.

The predominance of oxide ion conduction (as opposed to sodium ion or electronic conduction) is further confirmed by ^{18}O tracer diffusion measurements using isotopic exchange and line scanning by Secondary Ion Mass Spectrometry (SIMS), Fig. 3. For NBT at 632 ^oC, the tracer diffusion coefficient (D*) is 2.64×10^{-10} cm^2/s and the surface exchange coefficient (k*) is 2.97×10^{-9} cm/s. The diffusion profile is ~ 150 μm long, Fig. 3a, and since the grain size for this sample is 10-20 μm (Fig. S3), tracer species encounter numerous grains and grain boundaries. The conductivity calculated via the Nernst–Einstein equation from D* is ~ 1.1×10^{-4} S cm^{-1} is in agreement with the total (combined grain and grain boundary) resistivity value of ~ 9 kΩ cm obtained from IS data at 600 ^oC, Fig. 2b. The high tracer diffusion coefficient was confirmed by a second, independent analysis resulting in a D* of 5.24×10^{-10} cm^2/s at 608 °C (Fig. S5).

An obvious consequence of these results is to increase the ionic conductivity in NBT by increasing the concentration of oxygen vacancies by acceptor doping. 2 at% Mg-doping at the Ti-site (nominal composition $Na_{1/2}Bi_{0.49}Ti_{0.98}Mg_{0.02}O_{2.965}$) increases the diffusion coefficient by two orders of magnitude to $D^* = 1.17\times10^{-8}$ cm^2/s at 632 ^oC, Fig. 3b, which is close to the D^* value (2.29×10^{-8} cm^2/s) at 636 ^oC for the known perovskite oxide ion conductor $La_{0.9}Sr_{0.1}Ga_{0.9}Mg_{0.1}O_{2.9}$[16]. The calculated conductivity, ~ 5×10^{-3} S cm^{-1} is in excellent agreement with the measured IS value of ~ 8×10^{-3} S cm^{-1}, Fig. S6b and $t_i \geq 0.9$, Fig. 2d. The results of ^{18}O tracer diffusion measurements, combined with EMF measurements giving values close to unity for the transport number of oxygen, rules out any significant contribution from Na^+ ions or electronic conduction to the measured conductivity.

A comparison of bulk ionic conductivity for $Na_{1/2}Bi_{0.49}Ti_{0.98}Mg_{0.02}O_{2.965}$ and other known oxide ion conductors[16,17] is given in Fig. 4. The conductivity of NBT compares extremely well with those of the best oxygen-ion conducting electrolytes, and further improvements are expected with composition optimisation by appropriate A- and/or B-site doping. It should be noted that the large grain boundary arc observed in undoped conducting NBT with R_{gb} ~ 8 kΩcm in air at 600 ^oC, Fig. 2b, is heavily suppressed by 2 at% Mg doping, Fig. S6. At ~ 450 ^oC, the high frequency arc associated with the bulk response is similar in magnitude to the intermediate frequency arc associated with the grain boundary response, Fig. S6a; however, at ~ 500 ^oC and above, the grain boundary arc is considerably smaller in magnitude, Figs. S6a,b. This demonstrates a much higher E_a for grain boundary conduction compared to bulk conduction in $Na_{1/2}Bi_{0.49}Ti_{0.98}Mg_{0.02}O_{2.965}$ such that at ~ 600 ^oC the total conductivity of the ceramics is dominated by the bulk component, Fig. S6c.

Mg-doping has two other advantages. Firstly, the oxide ion conduction (electrolyte) window is extended to a much lower pO_2 range. Figs. 2b and 2d show no appreciable electronic conduction in NBT at 600 ^oC even in N_2. In reducing atmosphere ($5\%H_2/95\%N_2$), electronic conduction arises due to reduction of Ti^{4+} to Ti^{3+}, resulting in much smaller total resistivity, Fig. S7a-b. With just 1 at% Mg-doping on the Ti-site (nominal composition $Na_{1/2}Bi_{1/2}Ti_{0.99}Mg_{0.01}O_{2.99}$), R_b remains unchanged after ~ 45 hr in $5\%H_2/95\%N_2$ at 600 ^oC, Fig. S7c-d. Secondly, the sintering temperature of the ceramics can be significantly reduced to ~ 950 ^oC by 3-4 at% Mg-doping, Fig. S3.

The dominant oxide ion conduction in nominally stoichiometric and Bi-deficient NBT compositions is very surprising as the electrical conductivity in titanate-based perovskites is usually dominated by electronic conduction (electrons or holes) in most ranges of temperature and pO_2[18]. Although acceptor doping can lead to oxygen ionic conduction in perovskite titanates, significant levels of electronic conduction usually still persist[18]. There have been no reports of an oxide-ion conducting solid electrolyte based on a titanate perovskite. Why oxide ion conduction rather than electronic conduction is preferred in NBT is an interesting question and is discussed below. Firstly, in terms of the non-stoichiometry and defect chemistry of NBT and secondly, the origin of high oxygen-ion mobility in NBT.

The oxygen vacancies in nominal (starting) stoichiometric NBT composition may be generated during sample processing due to loss of Bi_2O_3:

$$2Bi_{Bi}^{x} + 3O_O^x \leftrightarrow 2V_{Bi}^{'''} + 3V_O^{\bullet\bullet} + Bi_2O_3 \qquad (1)$$

For compositions with a nominal starting Bi-deficiency (eg., $NBi_{0.49}T$), additional oxygen vacancies can be generated, leading to higher oxide ion conductivity, Fig. 1b.

The level of nonstoichiometry and oxygen vacancy concentration in conducting NBT compositions is low. Firstly, small amounts of secondary phase ($Na_2Ti_6O_{13}$) were observed in $NBi_{0.49}T$ by Scanning Electron Microscopy and Transmission Electron Microscopy revealed evidence of some Bi-rich regions at the triple points in $NBi_{0.51}T$, Fig. S2. Secondly, compositional analysis using both Energy Dispersive Spectrometry (EDS) at a local (grain) scale and Inductively Coupled Plasma - Atomic Emission Spectroscopy (ICP-AES) on the overall composition reveal no appreciable compositional differences between NBT, $NBi_{0.51}$ and $NBi_{0.49}T$, Table S1, within instrument resolution and standard deviation associated with these techniques. Thirdly, additional donor-doping experimental work shows 0.5 at% Nb-doping at the Ti-site is sufficient to fill the oxygen vacancies and increase the resistivity and Ea of NBT similar to that of $NBi_{0.51}T$, Fig. S8. These results imply the final composition of the nominal stoichiometric NBT composition after sintering has an oxygen vacancy concentration less than 0.25 at% and a bismuth vacancy concentration less than 0.17 at%., which corresponds to a formula of $Na_{1/2}Bi_{0.4983}TiO_{2.9975}$. For a nominal starting Bi-excess composition (eg., $Na_{1/2}Bi_{0.51}TiO_{3.015}$), Bi_2O_3 loss is compensated and the final bulk composition is close to stoichiometric $Na_{1/2}Bi_{1/2}TiO_3$. This sample is a dielectric and exhibits very low levels of electronic conduction. Unsurprisingly, such small composition variations can't be detected accurately by common chemical techniques. On the one hand, this is well known for many transition metal oxides, where low levels of nonstoichiometry (typically < 1at%) associated with impurities in raw materials, deliberate chemical doping and 'accidental' elemental loss during sample processing induce significant changes in electronic conductivity[18,19]. On the other hand, NBT is the first example to our knowledge to demonstrate that a small

compositional change in the A-site stoichiometry of an undoped perovskite can induce high levels of oxide ion conductivity.

The mobility of the oxygen ions must be high to obtain the level of oxide ion conductivity observed in NBT. The anion conduction pathway in perovskites is known to occur by a hopping mechanism where migrating anions pass through an opening (or bottleneck of critical radius) of a triangle defined between two A-site ions and a B-site ion, the so called saddle-point[20,21]. Computer simulations have shown the importance of cation polarisability in the conduction process as this can facilitate significant lattice relaxation and displacements of the cations away from the mobile oxygen ions[21]. This may be a crucial factor for the high oxide ion conductivity in NBT which contains a large amount of polarisable Bi-ions on the A-sites. There is hybridization of the bismuth $6s^2$ lone pair electrons and the oxygen 2p orbitals and this leads to weak Bi-O covalency with off-centring of Bi ions and a reduction in the co-ordination number which leads to a variety of Bi-O bond lengths for the non-cubic polytypes[12,13]. The highly polarised Bi^{3+} cations and weak Bi-O bonds are helpful for migration of oxygen ions. The softness of the polar and complex NBT lattice with its short and intermediate range cation and anion displacements, as revealed by TEM, Figs. S9 and S10, means it is a good structural host not only for piezo- and ferro-electric phenomena but also for oxide-ion conductivity.

This study also confirms generally accepted knowledge that the $6s^2$ lone pair electronic structure of Bi^{3+} ions plays a crucial role in anion migration of many Bi-based oxide ion conductors[22,23] and extends the class of close packed structures from fluorites such as δ-Bi_2O_3 to A-site Bi-based perovskites.

By adding a small excess of Bi_2O_3 to the starting composition, i.e. $Na_{1/2}Bi_{0.51}TiO_{3.015}$, oxygen vacancies are suppressed and electrical conductivity becomes much lower. Although our focus here is on the high oxide ion conductivity in acceptor-doped NBT, the results are also significant for the piezoelectric and multilayer ceramic capacitor communities in solving the origin of the high leakage conductivity problem and how to adjust the nominal NBT composition for dielectric-based applications.

Methods

Powders of NBT-based compositions with different stoichiometry were prepared using the solid state reaction method by double calcination at 800 and 850 ^{o}C for 2 h each. Dense ceramics were obtained by sintering for 2 h at 1150 ^{o}C for undoped compositions and at 950-1100 ^{o}C for Mg-doped NBT. X-ray diffraction (XRD), Scanning Electron Microscope (SEM), and Energy Dispersive X-ray Spectroscopy (EDS) were employed to examine the phase purity and ceramic microstructure. Electron diffraction patterns and ferroelectric domain structures were obtained using Transmission Electron Microscopy (TEM). Impedance Spectroscopy measurements were performed using Au or Pt paste electrodes. Oxygen ion transport number measurements on ceramics were performed at 600-800 ^{o}C using air/N_2 gas. ^{18}O tracer diffusion measurements were performed by annealing dense samples (relative density ~ 95-97%) in highly enriched $^{18}O_2$ gas. The oxygen isotope profiles were measured by means of Time-of-Flight Secondary Ion Mass Spectrometry (ToF-SIMS).

Full Methods and any associated references are available in the online version of the paper.

References:

1 Lacorre, P., Goutenoire, F., Bohnke, O., Retoux, R. & Laligant, Y. Designing fast oxide-ion conductors based on $La_2Mo_2O_9$. Nature **404**, 856-858 (2000).

2 Wachsman, E. D. & Lee, K. T. Lowering the temperature of solid oxide fuel cells. Science **334**, 935-939 (2011).

3 Steele, B. C. H. & Heinzel, A. Materials for fuel-cell technologies. Nature **414**, 345-352 (2001).

4 Kuang, X. et al. Interstitial oxide ion conductivity in the layered tetrahedral network melilite structure. Nat. Mater. **7**, 498-504 (2008).

5 Shao, Z. P. & Haile, S. M. A high-performance cathode for the next generation of solid-oxide fuel cells. Nature **431**, 170-173 (2004).

6 Ishihara, T., Matsuda, H. & Takita, Y. Doped $LaGaO_3$ perovskite type oxide as a new oxide ionic conductor. J. Am. Chem. Soc. **116**, 3801-3803 (1994).

7 Singh, P. & Goodenough, J. B. $Sr_{1-x}K_xSi_{1-y}Ge_yO_{3-0.5x}$: a new family of superior oxide-ion conductors. Energy Environ. Sci. **5**, 9626-9631 (2012).

8 Malavasi, L., Fisher, C. A. J. & Islam, M. S. Oxide-ion and proton conducting electrolyte materials for clean energy applications: structural and mechanistic features. Chem. Soc. Rev. **39**, 4370-4387 (2010).

9 Badwal, S. P. S. & Ciacchi, F. T. Ceramic membrane technologies for oxygen separation. Adv. Mater. **13**, 993-+ (2001).

10 Hiruma, Y., Nagata, H. & Takenaka, T. Thermal depoling process and piezoelectric properties of bismuth sodium titanate ceramics. J. Appl. Phys. **105**, 084112 (2009).

11 Sung, Y. S. et al. Effects of Bi nonstoichiometry in $Bi_{(0.5+x)}Na_{0.5}TiO_3$ ceramics. Appl. Phys. Lett. **98**, 012902 (2011).

12 Schütz, D. et al. Lone-pair-induced covalency as the cause of temperature- and field-induced instabilities in bismuth sodium titanate. Adv. Funct. Mater. **22**, 2285-2294 (2012).

13 Keeble, D. S. et al. Bifurcated polarization rotation in bismuth-based piezoelectrics. Adv. Funct. Mater. **23**, 185-190 (2012).

14 Levin, I. & Reaney, I. M. Nano- and mesoscale structure of $Na_{1/2}Bi_{1/2}TiO_3$: A TEM perspective. Adv. Funct. Mater. **22**, 3445-3452 (2012).

15 Bousquet, M. et al. Optical properties of an epitaxial $Na_{0.5}Bi_{0.5}TiO_3$ thin film grown by laser ablation: Experimental approach and density functional theory calculations. J. Appl. Phys. **107**, 104107 (2010).

16 Haavik, C., Ottesen, E. M., Nomura, K., Kilner, J. A. & Norby, T. Temperature dependence of oxygen ion transport in Sr plus Mg-substituted $LaGaO_3$ (LSGM) with varying grain sizes. Solid State Ionics **174**, 233-243 (2004).

17 Jung, D. W., Duncan, K. L. & Wachsman, E. D. Effect of total dopant concentration and dopant ratio on conductivity of $(DyO_{1.5})x$-$(WO_3)_y$-$(BiO_{1.5})_{1-x-y}$. Acta Mater. **58**, 355-363 (2010).

18 Smyth, D. M. The defect chemistry of metal oxides. (Oxford University Press, New York, 2000).

19 Kofstad, P. K. Nonstoichiometry, diffusion and electrical conductivity in binary metal oxides. (John Wiley & Sons Inc, New York, 1972).

20 Kilner, J. A. & Brook, R. J. A study of oxygen ion conductivity in doped non-stoichiometric oxides. Solid State Ionics **6**, 237-252 (1982).

21 Islam, M. S. Ionic transport in ABO_3 perovskite oxides: a computer modelling tour. J. Mater. Chem. **10**, 1027-1038 (2000).

22 Sammes, N. M., Tompsett, G. A., Nafe, H. & Aldinger, F. Bismuth based oxide electrolytes - Structure and ionic conductivity. J. Eur. Ceram. Soc. **19**, 1801-1826 (1999).

23 Aidhy, D. S., Sinnott, S. B., Wachsman, E. D. & Phillpot, S. R. Effect of ionic polarizability on oxygen diffusion in delta-Bi_2O_3 from atomistic simulation. Ionics **16**, 297-303 (2010).

Acknowledgements We thank the EPSRC for funding EP/G005001/1 and EP/K001329/1. Dr Denis Cumming (University of Sheffield) is acknowledged for helpful discussions and advice on EMF measurements. Mr Linhao Li (University of Sheffield) is acknowledged for assistance with sample preparation for EDS and ICP-AES analysis. Dr Neil Bramall (University of Sheffield) is acknowledged for ICP-AES analysis.

Author Contributions M.L. and D.C.S. conceived the idea of the project. M.L. prepared the samples, performed the XRD, SEM, Impedance Spectroscopy and oxygen transport number measurements. TEM analysis was performed by H.R.Z and I.M.R. ^{18}O tracer diffusion measurements were performed independently by M.J.P. and R.A.D.S. (Fig. 3) at RWTH Aachen University and S.N.C. and J.A.K. (Fig. S5) at Imperial College London. M.L. and D.C.S. wrote the manuscript. All authors commented on the manuscript. D.C.S. supervised the project.

Additional information

Supplementary information is available in the online version of the paper. Reprints and permissions information is available online at www.nature.com/reprints. Correspondence and requests for materials should be addressed to D.C.S.

Competing financial interests

The authors declare no competing financial interests.

Figure captions:

Fig. 1. (a) Z* plots for ceramics with nominal compositions $Na_{1/2}Bi_{1/2}TiO_3$ (NBT), $Na_{1/2}Bi_{0.49}TiO_{2.985}$ ($NBi_{0.49}T$) and $Na_{1/2}Bi_{0.51}TiO_{3.015}$ ($NBi_{0.51}T$) with Au electrodes at 500 ^oC. Inset in (a) shows high frequency data on an expanded scale. Filled symbols indicate selected frequencies; (b) Arrhenius-type plots of bulk conductivity for all samples.

Fig. 2. a) Z* plots for $Na_{1/2}Bi_{1/2}TiO_3$ with Au electrodes under different atmospheres at 600 ^oC; the inset shows the low frequency data on an expanded scale to highlight the response in air/O_2 compared to N_2; (b), high and intermediate frequency data of (a) on an expanded scale; the inset shows the highest frequency arc associated with the bulk response; (c), Z* plots for $NBi_{0.51}T$ with Au electrodes at 700 ^oC under different atmospheres. Filled symbols indicate selected frequencies; (d) oxygen ionic transport number, t_i, for various ceramics from Electromotive Force measurements using air/nitrogen gas.

Fig. 3. ^{18}O diffusion profile for $Na_{1/2}Bi_{1/2}TiO_3$ and $Na_{1/2}Bi_{0.49}Ti_{0.98}Mg_{0.02}O_{2.965}$ after exchange at 632 ^oC for 21883 s with $p^{18}O_2$ ~ 508 mbar.

Fig. 4. (a) Comparison of bulk oxide ion conductivity in the range ~ 200 to 600 ^oC of the nominal composition $Na_{1/2}Bi_{0.49}Ti_{0.98}Mg_{0.02}O_{2.965}$ and YSZ (8 at% Y_2O_3 stabilised ZrO_2, our own data), GDC ($Ce_{0.9}Gd_{0.1}O_{1.95}$, Ref. 17) and LSGM ($La_{0.9}Sr_{0.1}Ga_{0.9}Mg_{0.1}O_{2.9}$, Ref. 16)

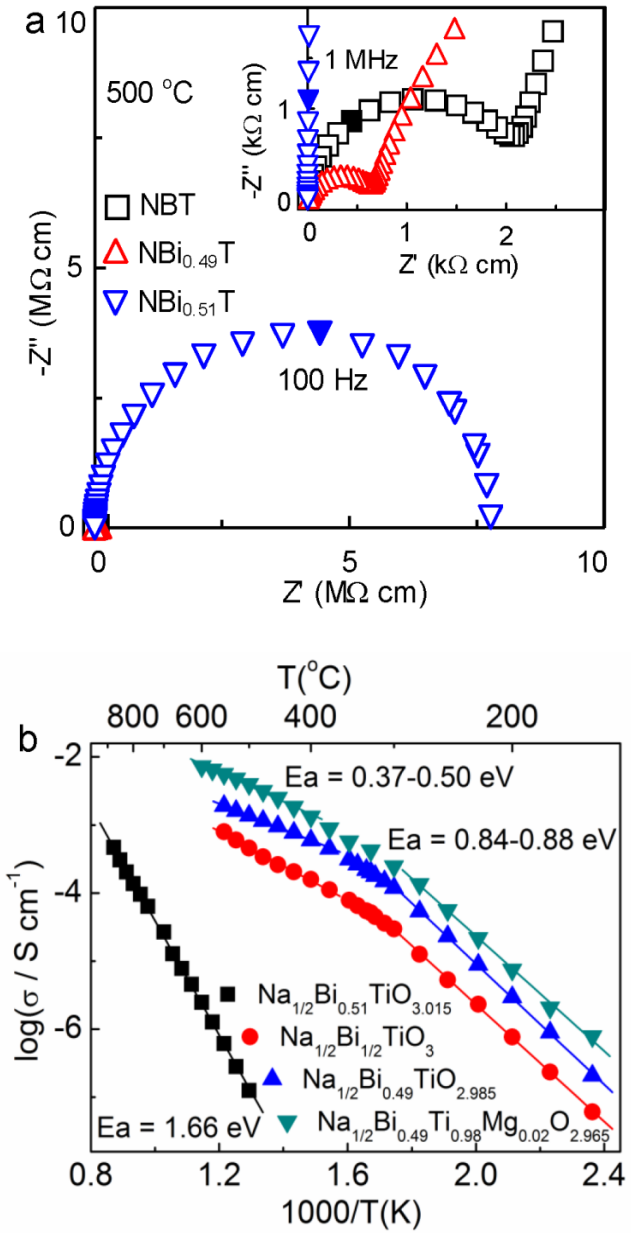
a
500 °C
NBT
NBi0.49T
NBi0.51T
100 Hz
1 MHz
-Z'' (MΩ cm)
Z' (MΩ cm)
-Z'' (kΩ cm)
Z' (kΩ cm)
b
T(°C)
800 600 400 200
Ea = 0.37-0.50 eV
Ea = 0.84-0.88 eV
Ea = 1.66 eV
Na1/2Bi0.51TiO3.015
Na1/2Bi1/2TiO3
Na1/2Bi0.49TiO2.985
Na1/2Bi0.49Ti0.98Mg0.02O2.965
log(σ / S cm-1)
1000/T(K)

Figure 1

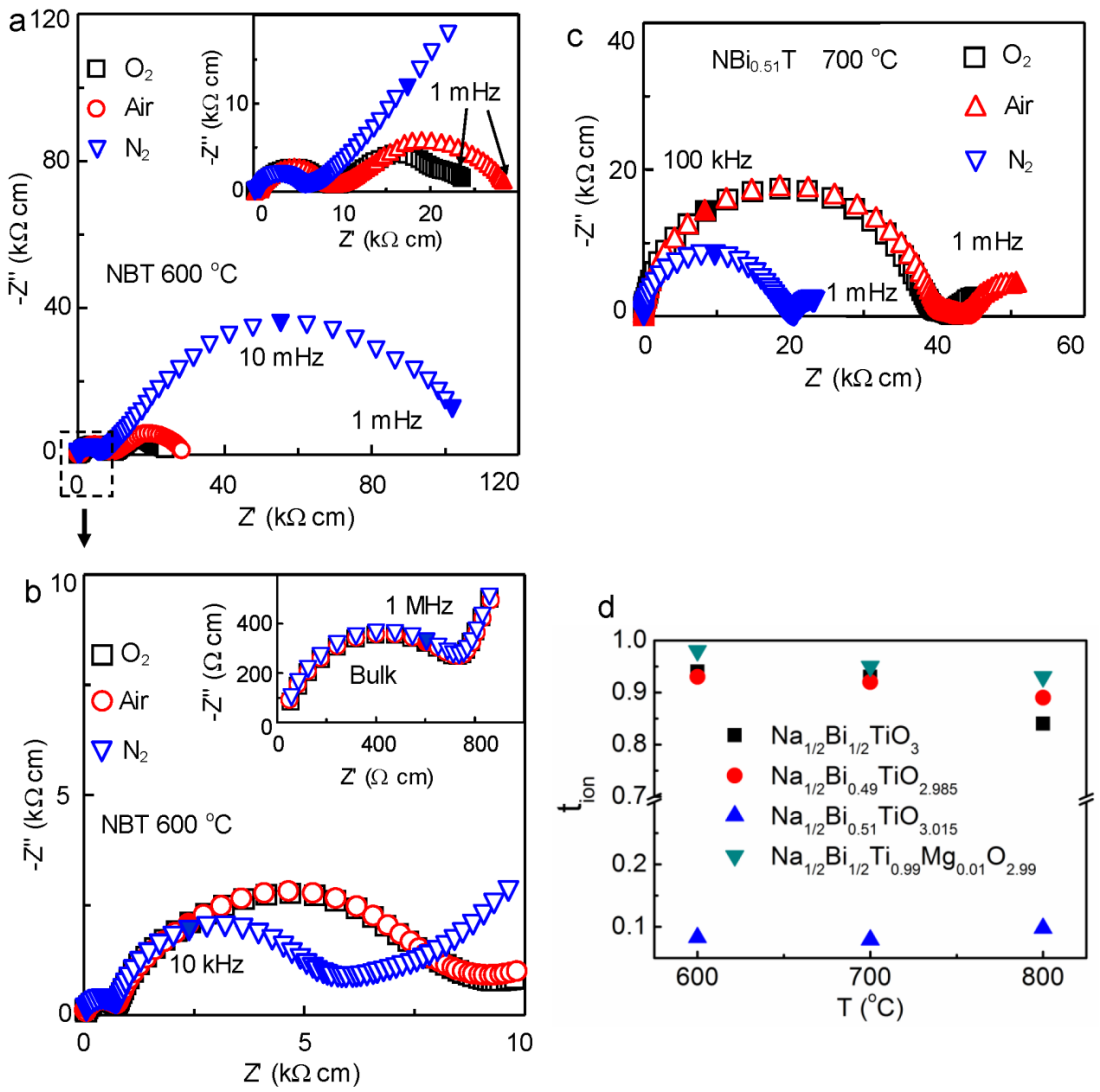
a
b
c
d
O2
Air
N2
NBT 600 °C
1 mHz
10 mHz
1 MHz
10 kHz
Bulk
NBi0.51T 700 °C
100 kHz
-Z'' (kΩ cm)
Z' (kΩ cm)
-Z'' (Ω cm)
Z' (Ω cm)
t_ion
T (°C)
Na1/2Bi1/2TiO3
Na1/2Bi0.49TiO2.985
Na1/2Bi0.51TiO3.015
Na1/2Bi1/2Ti0.99Mg0.01O2.99

Figure 2

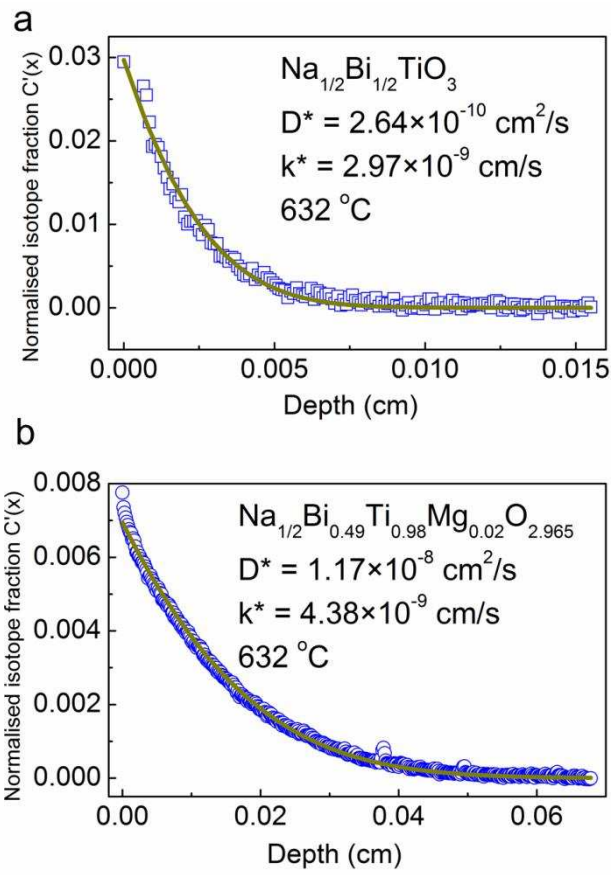
a
Normalised isotope fraction C'(x)
0.03
0.02
0.01
0.00
0.000
0.005
0.010
0.015
Depth (cm)
Na1/2Bi1/2TiO3
D* = 2.64×10-10 cm2/s
k* = 2.97×10-9 cm/s
632 °C
b
Normalised isotope fraction C'(x)
0.008
0.006
0.004
0.002
0.000
0.00
0.02
0.04
0.06
Depth (cm)
Na1/2Bi0.49Ti0.98Mg0.02O2.965
D* = 1.17×10-8 cm2/s
k* = 4.38×10-9 cm/s
632 °C

Figure 3

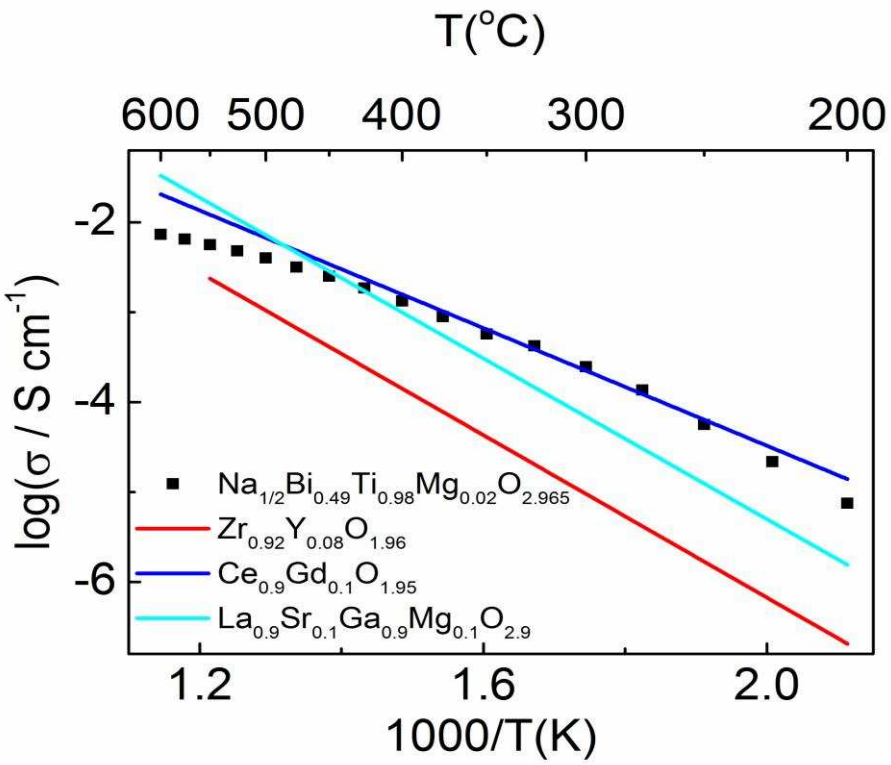
T(°C)
600 500 400 300 200
-2
-4
-6
log(σ / S cm-1)
Na1/2Bi0.49Ti0.98Mg0.02O2.965
Zr0.92Y0.08O1.96
Ce0.9Gd0.1O1.95
La0.9Sr0.1Ga0.9Mg0.1O2.9
1.2
1.6
2.0
1000/T(K)

Figure 4

Supplementary Information for

A family of oxide ion conductors based on the ferroelectric perovskite $Na_{1/2}Bi_{1/2}TiO_3$

Ming Li[1], Martha J. Pietrowski[2], Roger A. De Souza[2], Huairuo Zhang[1], Ian M. Reaney[1], Stuart N. Cook[3], John A. Kilner[3,4] and Derek C. Sinclair[1*]

[1]Department of Materials Science and Engineering, University of Sheffield, Sir Robert Hadfield Building, Mappin Street, Sheffield, S1 3JD, United Kingdom.

[2]Institute of Physical Chemistry, RWTH Aachen University and JARA-FIT, D-52056 Aachen, Germany.

[3]Department of Materials, Imperial College London, London, SW7 2AZ, United Kingdom.

[4]International Institute for Carbon-Neutral Energy Research (I2CNER), 744 Motooka Nishi-ku Fukuoka 819-0395, Japan.

* Author to whom correspondence should be addressed. E-mail: d.c.sinclair@sheffield.ac.uk.

Methods

Na_2CO_3 (99.5%), Bi_2O_3 (99.9%), TiO_2 (99.9%) and MgO (99%) were used as raw materials. Prior to weighing, Na_2CO_3, Bi_2O_3, TiO_2 and MgO were dried at 300, 180, 800 and 1000 ^oC for 8 h, respectively, followed by cooling in a vacuum desiccator. TiO_2 and MgO were cooled in a furnace down to 300 ^oC before being transferred to a desiccator. Mixtures of raw materials were ball milled using Y_2O_3-stabilised ZrO_2 grinding media for 6 h, dried, sieved and calcined at 800 ^oC for 2 h. The resultant powders were ball milled for 4 h followed by a second calcination at 850 ^oC for 2 h and ball milled for 6 h. Green bodies were first pressed in a uniaxial steel die and then isostatically pressed at 200 MPa, followed by sintering at 1150 ^oC for undoped compositions and at 950-1100 ^oC for Mg-doped NBT. All samples were sintered for 2 h in air. Prior to sintering the pellets were covered using powders of the same composition to reduce Na-and Bi-loss during the firing process. Pellet density was estimated by the Archimedes method and compared to that expected from the theoretical X-ray density.

Phase purity was checked by X-ray diffraction (XRD) using a high-resolution STOE STADI-P diffractometer (STOE & Cie GmbH, Darmstadt, Germany) operating with Cu $K\alpha_1$ radiation. Data were collected over the 2θ range 10-90° with a linear position sensitive detector (PSD).

Cross sections of pellets were polished, carbon-coated and examined using a Scanning Electron Microscope (SEM) JEOL 6400 (JEOL Ltd., Tokyo, Japan) equipped with an Oxford Link ISIS (Oxford Instruments Ltd., Oxfordshire, UK) Energy Dispersive X-ray Spectroscopy (EDS) detector. Grain compositions were obtained by EDS on polished samples (without thermal etching).

Average compositions of samples after sintering were measured by Inductively Coupled Plasma - Atomic Emission Spectroscopy (ICP-AES). The sintered pellets were crushed and ground into fine powders. The samples were then dissolved in 1% nitric acid and analysed by a Spectro-Ciros-Vision spectrometer (SPECTRO Analytical Instruments GmbH, Kleve, Germany).

Electron transparent Transmission Electron Microscopy (TEM) specimens were prepared by mechanical grinding followed by dimpling and ion-milling. TEM characterisation was performed using a Philips EM420 TEM (120 kV) and a JEOL 3010 TEM (300 kV), both equipped with high tilt angle specimen holders, as well as a JEOL 2010F TEM/STEM (200 kV) equipped with a high angle annular dark-field (HAADF) detector, an Oxford Instruments EDS system and Gatan Image Filter (GIF) system.

High temperature Impedance Spectroscopy (IS) measurements[1,2] were performed using an HP 4192A (Hewlett Packard, USA) Impedance bridge or a Solartron 1260 system (Solartron Analytical, United Kingdom) in a non-inductively wound tube furnace. Au paste (fired at 800 ^{o}C for 2 h) or Pt paste (fired at 900 ^{o}C for 1 h) electrodes were used. IS data were corrected for sample geometry (thickness/area of pellet) and analysed using ZView (Version 2.9c, Scribner Associates Inc., USA). Impedance data were corrected for the influence of high frequency instrumental-related (impedance analyser, lead, and sample jig) inductance by performing a short circuit measurement.

Oxygen ion transport number measurements on ceramics were performed using a ProboStat system (NorECs Norwegian Electro Ceramics AS, Oslo, Norway). The sample was sealed onto a YSZ tube using a commercial glass frit. An oxygen partial pressure, pO_2, difference was created across the ceramic by flowing N_2 into the YSZ tube and leaving the outside of the ceramic in air. The pO_2 difference was monitored by

measuring the voltage across the inner and outer electrodes on the YSZ tube. The voltage was measured using a Keithley 182 sensitive digital voltmeter. A schematic diagram of this set-up is shown in Fig. S1.

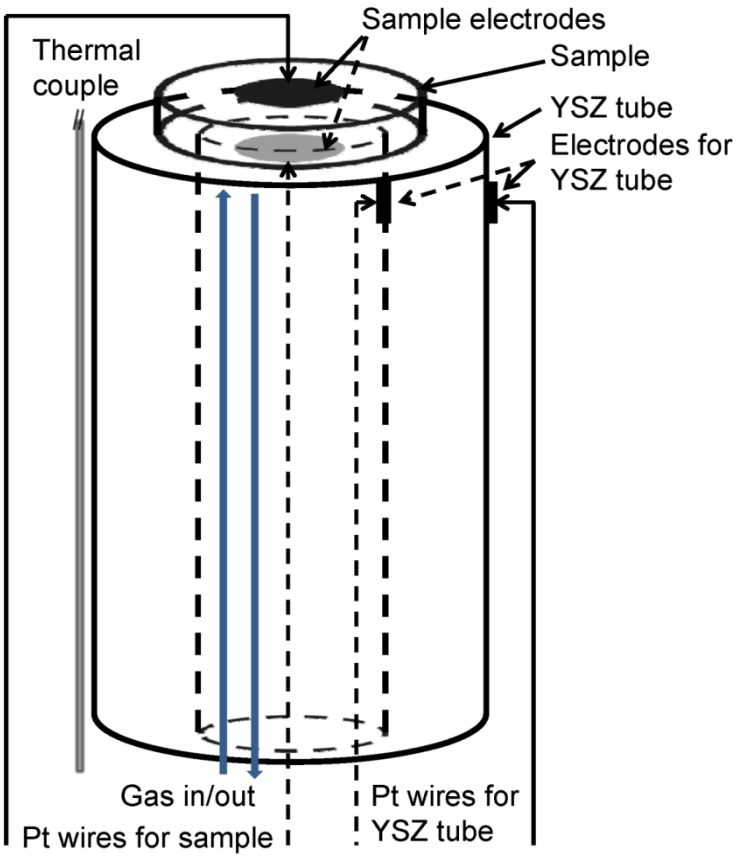

Fig. S1. Schematic diagram of the set-up used for EMF measurements.

^{18}O tracer diffusion measurements were performed independently at RWTH Aachen University by M.J.P. and R.A.D.S. (Fig. 3) and at Imperial College London by S.N.C. and J.A.K. (Fig. S5). The standard procedure for introducing an ^{18}O penetration profile into a solid from a large volume of gas was employed[3-5].

For both measurements, a sample was first equilibrated for a time t_{eq} ($t_{eq} \geqslant 10$ t) at the temperature and oxygen partial pressure of interest in oxygen of natural isotopic

abundance, and then quenched to room temperature. It was subsequently annealed for a time t, in highly ^{18}O-enriched gas at the same temperature and oxygen partial pressure. Given the lengths of the ^{18}O penetration profiles (> 10 µm), the samples were cut perpendicular to the original surface and the exposed cross-section polished for Secondary Ion Mass Spectrometry (SIMS) analysis. Measurements at RWTH Aachen University were performed at a temperature of 632 °C, ~500 mbar, while those at Imperial College London were performed at 608 °C, ~750 mbar, with the addition of a silver coating, sintered at 700 °C for 2 h, facilitating a high level of surface oxygen exchange.

The oxygen isotope profiles in the NBT samples were measured by means of Time-of-Flight Secondary Ion Mass Spectrometry (ToF-SIMS). Utilized equipment at RWTH Aachen consisted of a ToF-SIMS IV machine (IONTOF GmbH, Münster, Germany), equipped with a high-energy Ga^+ gun for producing secondary ions for ToF analysis, a low-energy Cs^+ gun for sputter etching of the sample, and a low-energy electron flood gun for charge compensation. The Ga^+ gun was operated in burst mode, with an ion energy of 25 keV, an analysis raster of 500 µm × 500 µm, and a cycle time of 60 µs. Charge compensation was accomplished with < 20 eV electrons. Measurements at Imperial College London were performed on a ToF-SIMS V instrument (IONTOF GmbH, Münster, Germany), equipped with a high-energy Bi^+ gun (operated in burst alignment mode with 8 pulses at 25 keV), a low-energy Cs^+ gun (operated at 2 keV) for sputter etching of the sample, and a low-energy electron flood gun for charge compensation. 200 µm × 200 µm ion images were collected. In all cases, after sputter cleaning of the sample surface with Cs^+ ions, a series of oxygen isotope images were acquired; negative secondary ions were detected. The pressure in the main chamber of the SIMS machine was below 10^{-8} mbar during all analyses.

Phase purity analysis by XRD, SEM and TEM

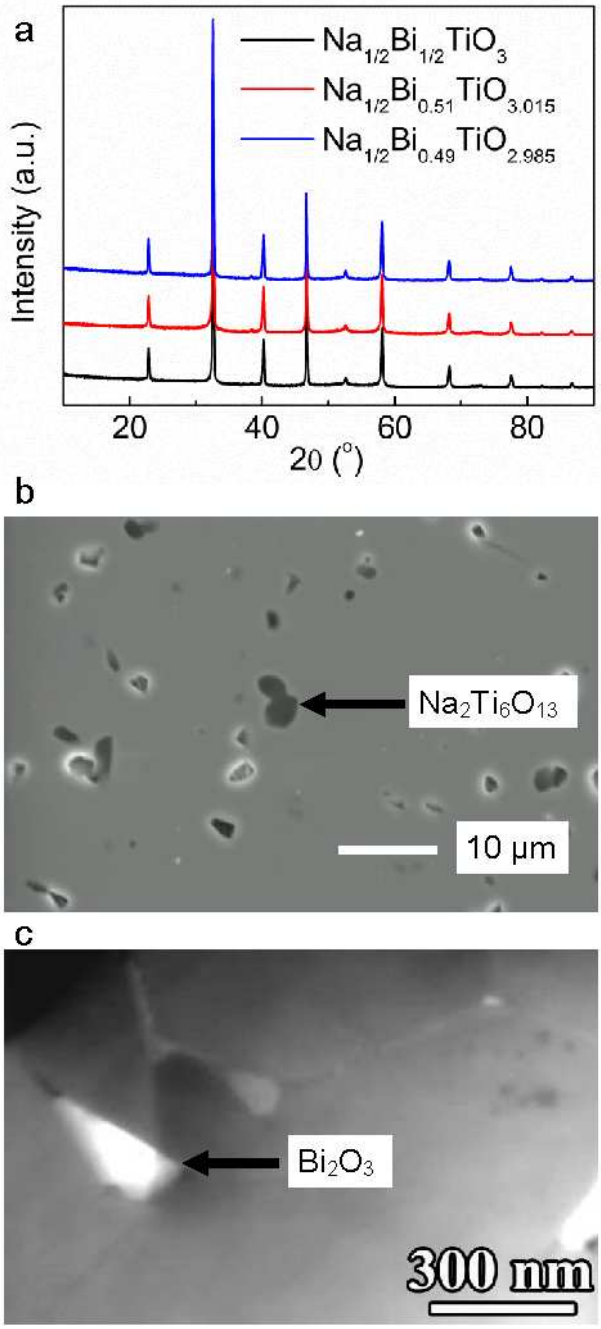

Fig. S2. (a) XRD patterns of NBT, $NB_{0.49}T$ and $NB_{0.51}T$ after double calcination at 800 and 850 ^{o}C for 2 h; (b) Secondary electron image of a $NB_{0.49}T$ ceramic (polished without thermal etching) with the dark arrowed region showing the presence of the secondary phase $Na_2Ti_6O_{13}$; (c) HAADF Z-contrast image showing some Bi-rich precipitates (arrowed white areas) at the triple points in $NB_{0.51}T$.

No secondary phase was observed in NBT, $NB_{0.49}T$ and $NB_{0.51}T$ by XRD, Fig. S2a. SEM results revealed small amounts of $Na_2Ti_6O_{13}$ in $NB_{0.49}T$, Fig. S2b and TEM revealed evidence of some Bi-rich regions at the triple points in $NB_{0.51}T$, Fig. S2c.

Ceramic Microstructure

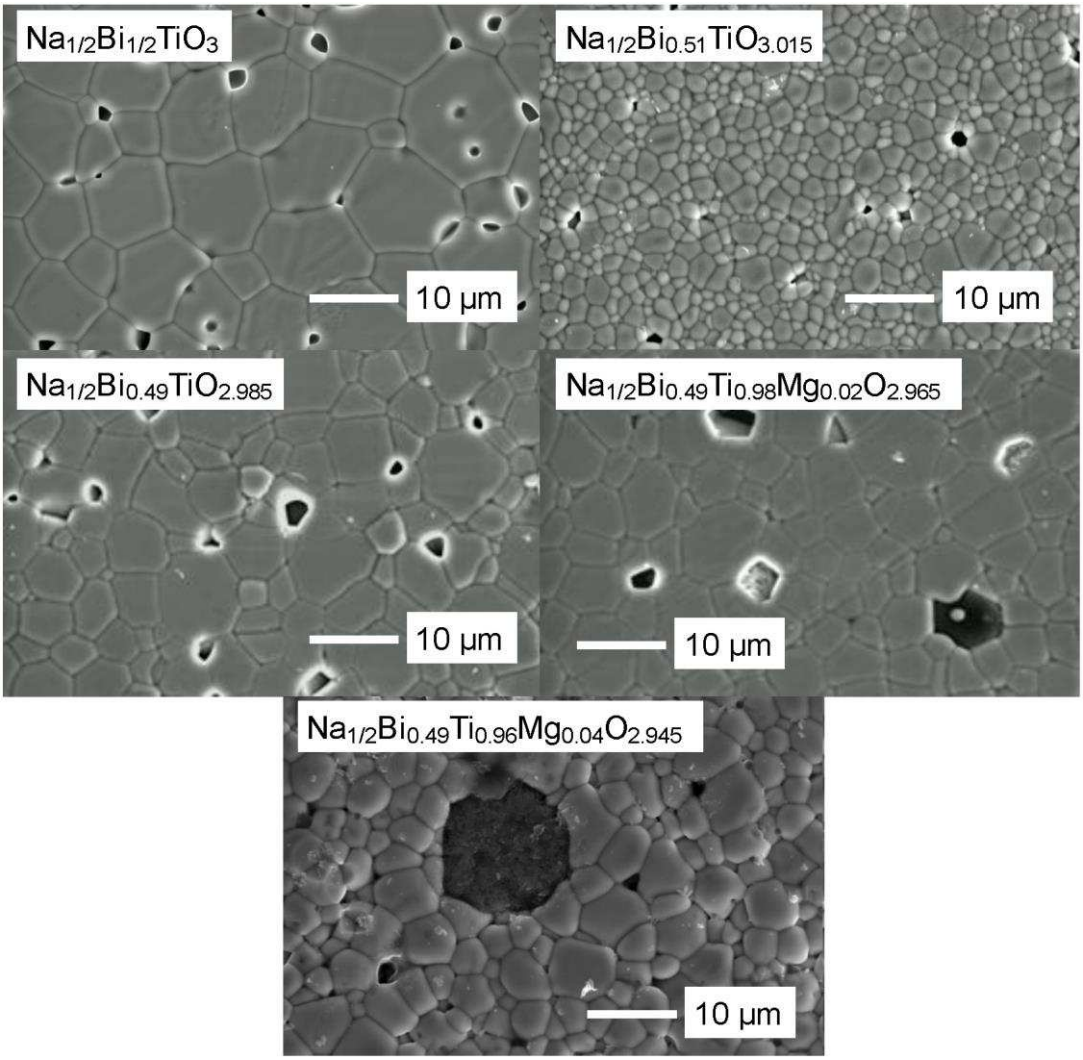

Fig. S3. SEM micrographs of selected samples. All were polished and thermally etched prior to SEM. NBT, $NBi_{0.49}T$ and $NBi_{0.51}T$ ceramics were sintered at 1150 ^oC for 2 h. $Na_{1/2}Bi_{0.49}Ti_{0.98}Mg_{0.02}O_{2.965}$ and $Na_{1/2}Bi_{0.49}Ti_{0.96}Mg_{0.04}O_{2.945}$ ceramics were sintered at 1100 and 950 ^oC for 2 h, respectively.

All samples exhibit high density (relative density > ~ 95%). NBT ceramics exhibit grain size ~ 10-20 μm. For the starting Bi-deficient and Mg-doped samples, the grain size is slightly smaller. Small amounts of secondary phase (dark regions) are observed by SEM in 2 at% and 4 at% Mg-doped NBT samples. Based on EDS spectra, one of the main cations in the secondary phase is Ti. The other main cation(s) may be Na or Mg or both, as the Kα energy for Na (1.04 keV) and Mg (1.25 keV) is similar. The grain size for the starting Bi-excess sample shows a clear decrease in grain size to < 5 μm. It is noted that Mg-doping improves ceramic sinterability. With 4 at% Mg-doping (nominal composition $Na_{1/2}Bi_{0.49}Ti_{0.96}Mg_{0.04}O_{2.945}$), dense ceramics can be obtained at 950 ^{o}C.

Compositional analysis

Samples were analysed by EDS and ICP-AES and the cation ratios are normalised to 100% in Table S1. For stoichiometric NBT, the theoretical Na, Bi and Ti percentage is 25.00 at%, 25.00 at% and 50.00 at%, respectively. The measured compositions of NBT, $NaBi_{0\text{-}51}T$ and $NaBi_{0\text{-}49}T$ by EDS and ICP-AES are close to the cation ratio in NBT within instrument resolution and standard deviations. Focussing on the A-site non-stoichiometry in the undoped samples, the theoretical Na/Bi ratio for NBT, $NB_{0.51}T$ and $NB_{0.49}T$ should be 1.00, 0.98 and 1.02, respectively. EDS and ICP-AES give values of 0.99 and 1.00 for NBT, 0.97 and 1.00 for $NB_{0.51}T$, and 1.00 and 1.04 for $NB_{0.49}T$, respectively and are all within the standard deviations associated with the measurements. It is challenging to unambiguously distinguish these three samples with such small differences in the starting composition. The insensitivity of common chemical techniques to such small composition variations make it difficult to link the final compositions for each sample with their electrical properties, as commonly observed when studying the relationship between composition and electrical properties in many

other transition metal oxides[6,7]. For Mg-doped NBT ($Na_{1/2}Bi_{0.49}Ti_{0.98}Mg_{0.02}O_{2.965}$), the measured Mg content by ICP-AES (0.94 at%) is close to nominal level (1.0 at%), whereas EDS results reveal only 0.50 at% Mg in the bulk phase. This either suggests the Mg-doping level is limited or is related to a measurement problem due to the proximity of Kα lines for Na (1.04 keV) and Mg (1.25 keV) as discussed above.

Table S1, Local and average compositions by EDS and ICP-AES, respectively. EDS data were obtained by measurements on 6-10 randomly selected areas. The mean value and standard deviation are listed. For ICP-AES analysis, three reading were recorded and the mean value is given. The relative standard deviation is typically 1-2%.

	Na (at%)	Bi (at%)	Ti (at%)	Mg (at%)
EDS				
NBT	25.03 (±0.43)	25.17 (±0.21)	49.80 (±0.36)	
$NaBi_{0.51}T$	24.71 (±0.40)	25.43 (±0.36)	49.85 (±0.41)	
$NaBi_{0.49}T$	25.08 (±0.32)	24.98 (±0.13)	49.94 (±0.26)	
$Na_{1/2}Bi_{0.49}Ti_{0.98}Mg_{0.02}O_{2.965}$	25.52 (±0.34)	24.90 (±0.20)	49.09 (±0.36)	0.50 (±0.26)
ICP-AES				
NBT	25.01	24.93	50.07	
$NaBi_{0.51}T$	24.94	24.73	50.33	
$NaBi_{0.49}T$	25.13	24.22	50.65	
$Na_{1/2}Bi_{0.49}Ti_{0.98}Mg_{0.02}O_{2.965}$	25.04	24.26	49.76	0.94

Dielectric properties

The temperature dependence of relative permittivity at 1 MHz for NBT, $NBi_{0.49}T$ and $NBi_{0.51}T$, Fig. S4a, are similar to that reported in the literature.[8,9] There is no significant difference between the three samples. The dielectric loss (tan δ) of NBT, $NBi_{0.49}T$ increases sharply above ~ 300 ^{o}C and is significantly larger than that of $NBi_{0.51}T$. The latter exhibits very low tan δ (< 0.03) at 300 – 600 ^{o}C, indicating this is a good dielectric material. The sharp contrast in dielectric loss between NBT and $NBi_{0.49}T$ with $NBi_{0.51}T$ is related to the high oxide-ion conductivity in the former as compared to the latter, Figs. 1, 2 and 3.

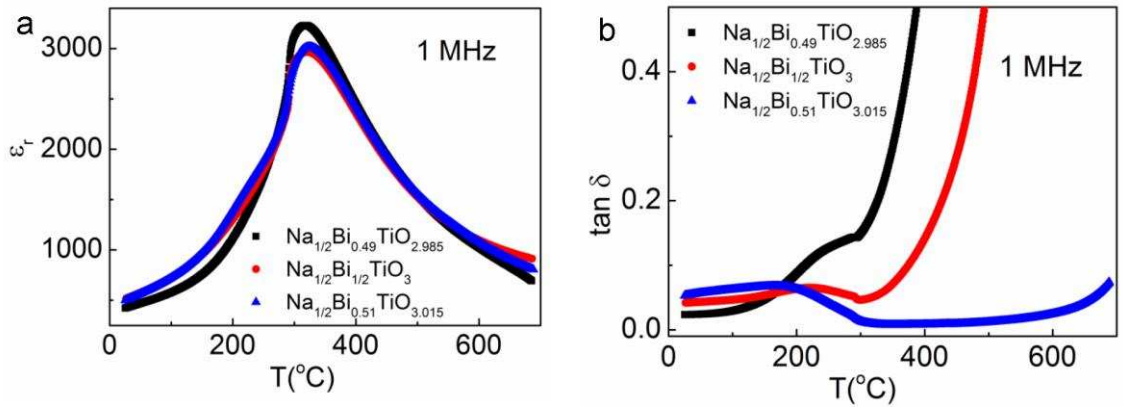

Fig. S4, temperature dependence of, (a) relative permittivity and, (b), tan δ at 1 MHz for NBT, $NBi_{0.49}T$ and $NBi_{0.51}T$.

The ε_r values of ~ 1600 – 1700 in Table S2 obtained from the Z* plots of Impedance Spectroscopy data at 500 ^{o}C in Fig. 1a for the various undoped samples are in excellent agreement with the value of ~ 1500 at 500 ^{o}C obtained from the fixed frequency (1 MHz) capacitance data shown in Fig. S4a. This confirms the assignment of the high frequency arc in Z* plots to be a bulk (grain) response.

Table S2, extracted bulk resistivity, R_b, and relative permittivity, ε_r, from the high frequency arc shown in the Z* plots, Fig. 1a. ε_r is calculated from $\varepsilon_r = C/\varepsilon_0$ where C is the extracted capacitance from the arc (using the relationship $\omega RC=1$ at the arc maximum where $\omega = 2\pi f$ and f is the frequency (in Hz) at the arc maximum) and corrected for sample geometry and ε_0 is the permittivity of free space, 8.854×10^{-14} F cm^{-1}.

	$Na_{1/2}Bi_{1/2}TiO_3$	$Na_{1/2}Bi_{.051}TiO_{3.015}$	$Na_{1/2}Bi_{0.49}TiO_{2.985}$
R_b (Ωcm)	2.2×10^3	8.0×10^6	0.72×10^3
ε_r	1626	1694	1649

Second, independent ^{18}O tracer diffusion measurement

The tracer diffusion coefficient (D*) at 608 °C is 5.24×10^{-10} cm^2/s is reasonably close to the value of 2.64×10^{-10} cm^2/s at 632 ^oC obtained by M.J.P. and R.A.D.S. at RWTH Aachen University (Fig. 3). The surface exchange coefficient (k*) is 1.73×10^{-6} cm/s, which is three orders of magnitude higher than that (2.97×10^{-9} cm/s) obtained by M.J.P. and R.A.D.S. Such an enhancement of surface kinetics is due to the previously discussed application of Ag to the sample surfaces.

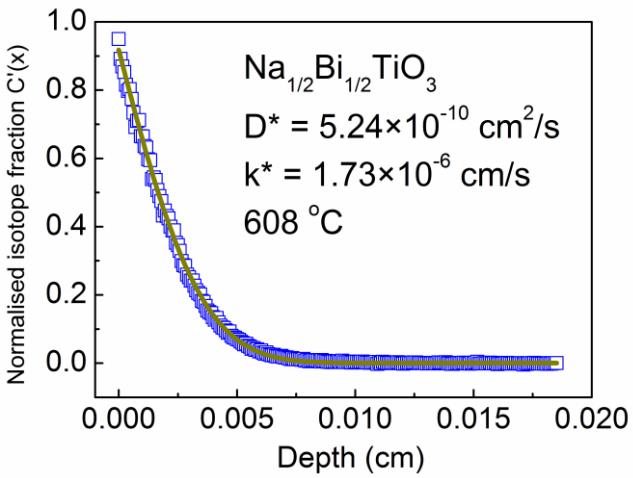

Fig. S5, ^{18}O diffusion profile for $Na_{1/2}Bi_{1/2}TiO_3$ after exchange at 608 ^{o}C for 8040 s with $p^{18}O_2$ ~ 750 mbar. Measurements were performed by S.N.C. and J.A.K at Imperial College London.

$La_{2/3-x}Li_{3x}TiO_3$ is a well-known solid solution perovskite phase with high levels of Li^+ conduction at x ~ 0.1 where migration of the Li^+ ions occurs via vacant A-sites[10]. In contrast, $Na_{1/2}La_{1/2}TiO_3$ is an electrically insulating perovskite that is a quantum paraelectric[11]. Given the low levels of A-site non-stoichiometry in NBT it is pertinent to consider the possibility of Na^+ ion conductivity in NBT, however, the pO_2 dependence of the Impedance Spectroscopy results (Fig. 2a-b), the magnitude of the EMF transport measurements (Fig. 2d) and ^{18}O tracer diffusion data (Fig. 3 and Fig. S5) support O^{2-} ions as opposed to Na^+ ions as the major mobile species and therefore the main charge carrier in conducting samples of NBT.

Effect of Mg-doping on grain boundary resistivity

NBT ceramics exhibit large grain boundary resistance, Fig. 2b. Mg-doping is helpful to minimise the grain boundary contribution to the total resistivity, as demonstrated by Z* plots at different temperatures for $Na_{1/2}Bi_{0.49}Ti_{0.98}Mg_{0.02}O_{2.965}$, Fig. S6. At 450 ^{o}C, an intermediate frequency grain boundary arc is clearly observed, Fig. S6a. With increasing temperature the magnitude of the grain boundary arc decreases much rapidly than the grain arc. At 600 ^{o}C the grain boundary arc is barely resolved in the Z* plot and the grain boundary contribution to the total sample resistivity is negligible. It should be noted that the low frequency arc at 600 ^{o}C is related to an electrode response. Arrhenius-type plots of conductivity show the activation energy for conduction, Ea, is higher for the grain boundaries (1.07 eV) as compared to that of the grains (0. 43 eV).

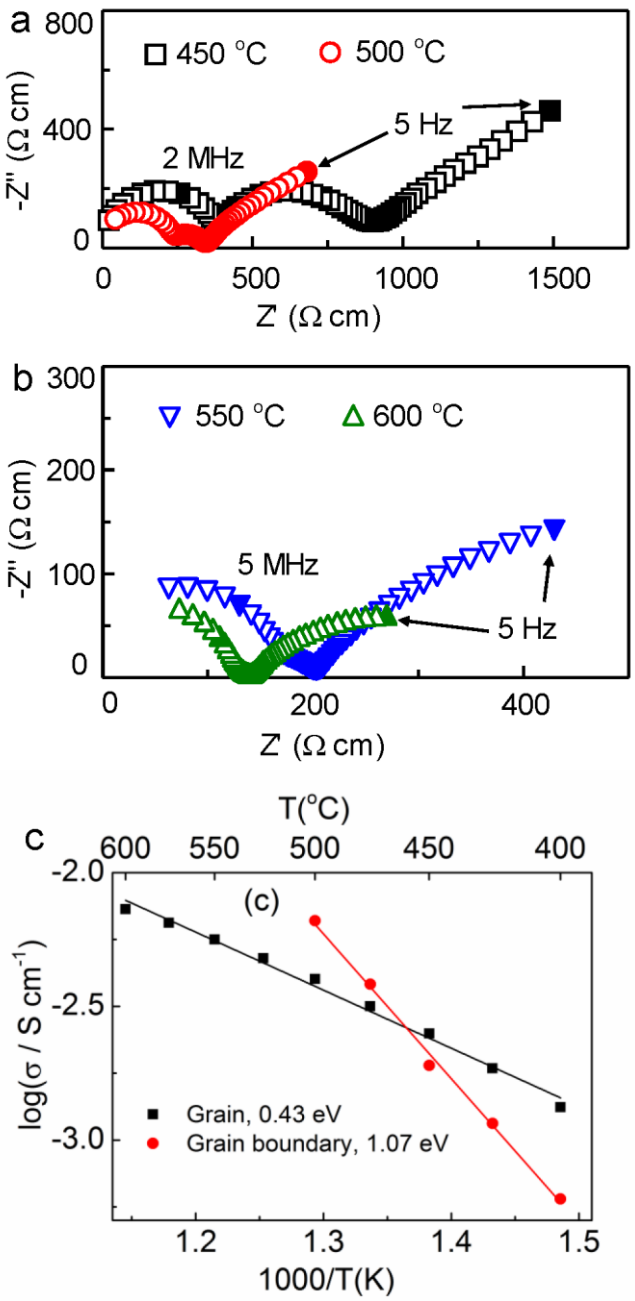

Fig. S6, Z* plots for $Na_{1/2}Bi_{0.49}Ti_{0.98}Mg_{0.02}O_{2.965}$ at (a) 450 and 500 ^{o}C, (b), 550 and 600 ^{o}C; (c) Arrhenius-type plots of the grain and grain boundary conductivity for $Na_{1/2}Bi_{0.49}Ti_{0.98}Mg_{0.02}O_{2.965}$.

Increased electrolyte domain for oxide ion conduction by Mg-doping

Many titanates exhibit p-type electrical conduction at higher pO_2 that switches to n-type conduction at lower pO_2.[7] The p-type behaviour is typically related to low levels of acceptor-type impurities/dopants. For example, oxygen vacancies are created according to the following reaction:

$$A_2O_3 \leftrightarrow 2\,A_{Ti}' + 3\,O_O^x + V_O^{\bullet\bullet} \qquad (1)$$

At high oxygen activity p-type conduction occurs by the following reaction:

$$\frac{1}{2}O_2 + V_O^{\bullet\bullet} \leftrightarrow O_O^x + 2h^{\bullet} \qquad (2)$$

In a reducing atmosphere, n-type conduction occurs due to a low level of anion nonstoichiometry associated with oxygen loss, accompanied by partial reduction of Ti^{4+} to Ti^{3+} ions by the following reactions:

$$O_O^x \leftrightarrow V_O^{\bullet\bullet} + 2e' + \frac{1}{2}O_2 \qquad (3)$$

$$2Ti^{4+} + 2e' \leftrightarrow 2Ti^{3+} \qquad (4)$$

In NBT, there is no change in bulk electrical conductivity at 600 ^oC by varying the pO_2 from O_2 to N_2. This is in sharp contrast to many other known titanates such as $BaTiO_3$.[7] Nevertheless, NBT becomes reduced in $5\%H_2/95\%N_2$ at 600 ^oC, resulting in much higher electronic conductivity. The bulk and grain boundary responses shift above the upper limit of the measured frequency range. The extracted capacitance from the arc in Fig. S7b is ~ 50 $\mu F\ cm^{-1}$, suggesting it is related to an electrode response. The non-zero intercept at high frequency is assigned as the total resistivity of NBT.

With just 1 at% Mg-doping, there is no change observed in bulk resistivity at 600 ^{o}C in 5%H_2/95%N_2 for 45 h, Fig. S7d, despite a small increase in grain boundary resistivity, Fig. S7c.

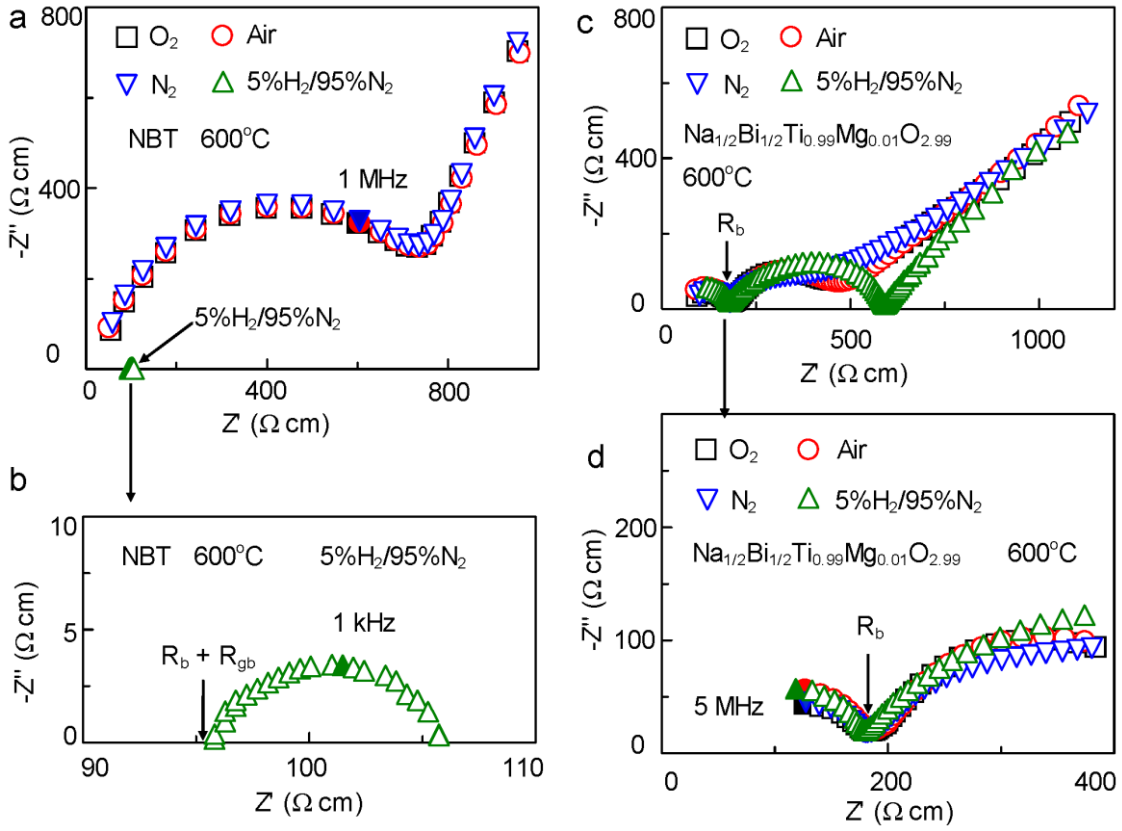

Fig. S7, (a) Z* plots for NBT at 600 ^{o}C under different atmospheres, (b) expanded scale for the data in 5%H_2/95%N_2, (c) Z* plots for $Na_{1/2}Bi_{1/2}Ti_{0.99}Mg_{0.01}O_{2.99}$ at 600 ^{o}C under different atmospheres, and (d) expanded scale for the high frequency data.

Effect of donor doping on the electrical properties of NBT

Based on the defect chemistry discussed in the main paper, it is expected that donor doping (such as Nb^{5+} at Ti-site) can fill the oxygen vacancies generated by Bi loss and suppress the oxide ion conductivity, equation 5-6:

$$2\,Bi_{Bi}^{x} + 3O_o^{x} \leftrightarrow 2\,V_{Bi}^{///} + 3\,V_o^{\bullet\bullet} + Bi_2O_3 \qquad (5)$$

$$Nb_2O_5 + Vo^{\bullet\bullet} \leftrightarrow 2Nb_{Ti}^{\bullet} + 5O_o^{x} \qquad (6)$$

This idea is confirmed by additional experimental work on Nb-doping. 0.5 at% Nb doping (nominal composition $Na_{1/2}Bi_{1/2}Ti_{0.995}Nb_{0.005}O_{3.0025}$) is sufficient to make NBT insulating, exhibiting similar resistivity and Ea to that of $NaBi_{0.51}T$, Fig. S8, which supports the suggestion that the bismuth and oxygen vacancy concentrations in our starting stoichiometric NBT is low. From equations 5-6 it follows that the oxygen vacancy concentration is < 0.25 at% and therefore the bismuth vacancy concentration is < 0.17 at%. The electrical data from the Nb-doping studies are consistent with SEM/TEM results in Fig. S2 and compositional data in Table S1 that show the nonstoichiometry level in NBT is low.

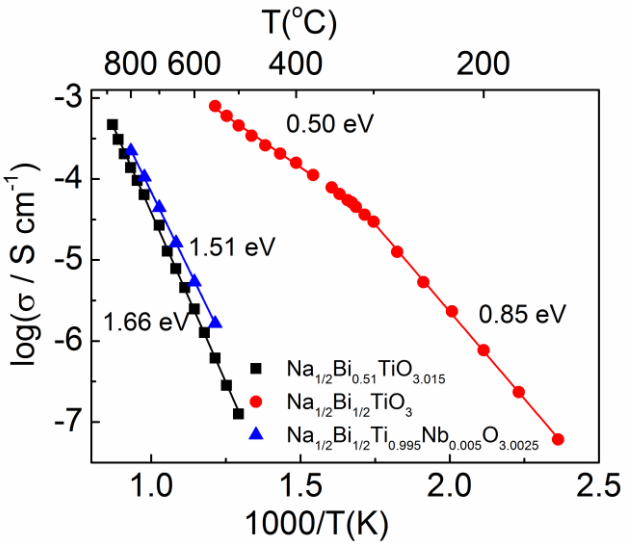

Fig. S8, Arrhenius-type plots of bulk conductivity for nominal compositions of $Na_{1/2}Bi_{1/2}TiO_3$, $Na_{1/2}Bi_{0.51}TiO_{3.015}$ and $Na_{1/2}Bi_{1/2}Ti_{0.995}Nb_{0.005}O_{3.0025}$.

Crystal structure and ferroelectric domain structures

NBT has an ABO_3 perovskite-type structure but the crystal chemistry is complex with differences in the average and local structure being reported depending on the characterisation techniques used and whether the samples are ceramics or single crystals[12-22]. On an average scale, based on neutron powder diffraction studies[12], NBT is reported to exhibit a sequence of phase transitions (on cooling) from a high temperature cubic (space group $Pm\bar{3}m$), to tetragonal (space group, Pb4m) and then to a room temperature (RT) rhombohedral (space group R3c) structure. More recently, high-resolution synchrotron powder x-ray diffraction data reveal the RT structure to be monoclinic (space group, Cc)[13-15]. A recent Transmission Electron Microscopy study on ceramics additionally revealed significant chemical, cation-displacement and tilt disorder of the NBT structure at the nano and mesoscale[16]. In particular, octahedral tilting was studied at length by the authors of Ref. 16 who concluded that NBT is best described by a single-phase 'continuous tilting' model in which each orthogonal axis exhibits short range-ordered in-phase ($a^-a^-c^+$) tilting superimposed on long-range ordered anti-phase ($a^-a^-c^-$) tilting. This continuous tilting model is consistent with the 'average' monoclinic structure recently proposed from powder diffraction[14]. The intrinsic disorder and softness of the NBT lattice are crucial factors for its functionality as a polar dielectric material.

Typical [310] zones axis electron diffraction patterns (EDPs) from NBT and Mg-doped NBT are shown in Fig. S9. The distribution of intensities in Fig. S9 and the presence and nature of the diffuse scatter is qualitatively similar to that reported and described in Ref. 16 and indicates a high degree of disorder associated with the rotations of the oxygen octahedra, consistent with a 'continuous tilting' model. However, the streaked

intensities along [001] in Mg-doped NBT are discernibly stronger under nominally similar imaging conditions (approximately the same sample thickness, illumination spread and beam intensity) than those in undoped samples (NBT and $NB_{0.51}T$). Fig. S10 presents dark field images from stoichiometric NBT and Mg-doped NBT obtained using ½{1 $\bar{3}$ 1} reflections. The stoichiometric NBT reveals classic antiphase boundaries (APBs), defined by regions of antiphase octahedral rotations that have nucleated out of phase and impinged, as well as conventional ferroelastic/ferroelectric twin domains. These images are similar to those reported by Reaney and Levin[16] and typical of ceramic NBT. The equivalent image from Mg-doped NBT however, shows a highly disorder planar defect structure with a complex arrangement of APBs and twin domains. In Mg-doped NBT, the presence of Mg at the Ti-site, $Mg_{Ti}^{//}$, and resultant much higher concentration of oxygen vacancy, $V_O^{\cdot\cdot}$, increase the domain nucleation density and induce greater tilt and long range cation displacement (polar) disorder, giving rise to a distinct increase in intensity of streaking along [001].

Although oxygen ion conduction in, for example, NBT is greater than that in $NB_{0.51}T$, there is little qualitative difference in their planar defect structure and diffraction data. Subtle changes in the kinematic intensity of streaking $NB_{0.51}T$ and NBT may well be present arising from changes in scale length and degree of oxygen octahedral and cation displacement order but dynamical scattering makes unambiguous interpretation unreliable.

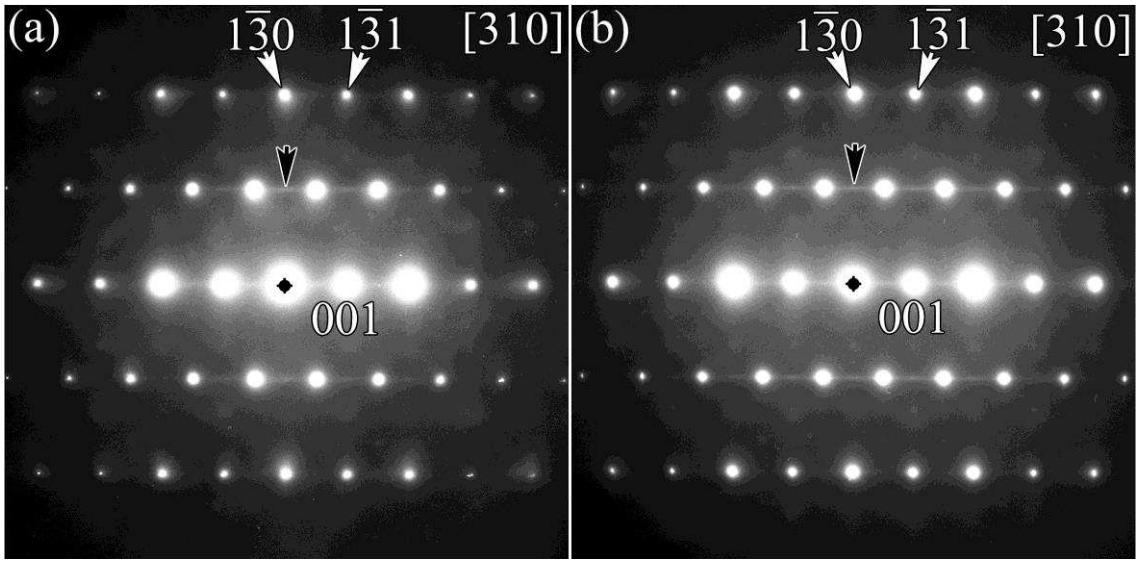

Fig. S9. (a) NBT and (b) Mg-doped NBT [310] pseudo-cubic zone-axis electron diffraction patterns showing the diffuse scattering streaks running along the <001> direction, and the strong 1/2(ooo) antiphase tilting reflections between the fundamental pseudo-cubic reflections. Weak enhancement of the streaking is observed at ½{ooe} positions.

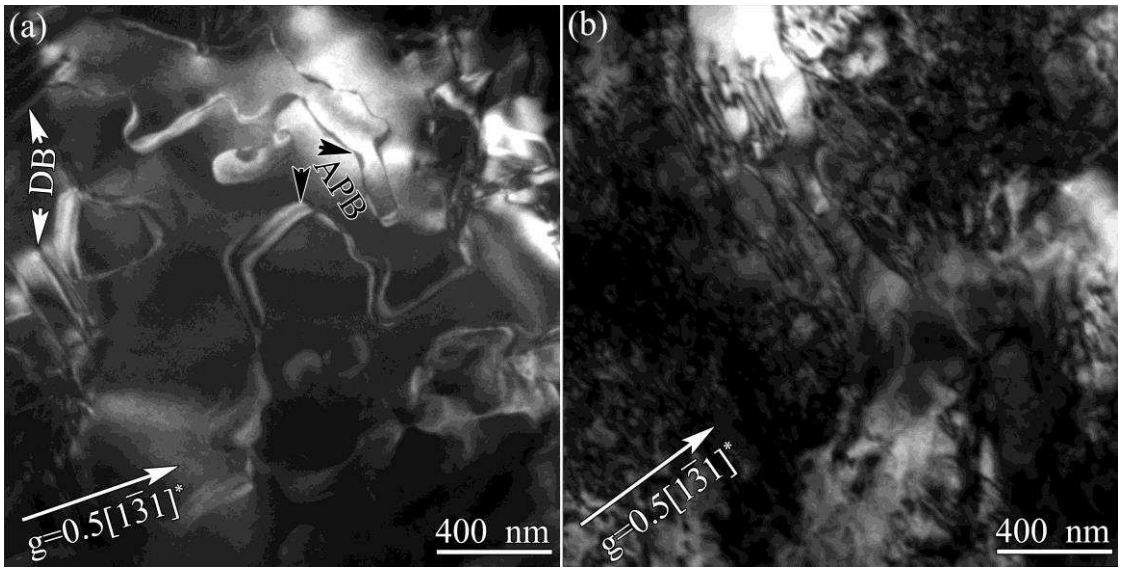

Fig. S10. (a) NBT and (b) Mg-doped NBT dark field images obtained near the [310] zone-axis with g=1/2[1$\bar{3}$1]*. The white arrows in (a) indicate the ferroelastic domain boundaries (DBs) and black arrows antiphase boundaries (APBs), in (b) there is higher density of DBs and APBs.

References

1 Irvine, J. T. S., Sinclair, D. C. & West, A. R. Electroceramics: characterization by impedance spectroscopy. Adv. Mater. **2**, 132-138 (1990).

2 Sinclair, D. C. & West, A. R. Impedance and modulus spectroscopy of semiconducting $BaTiO_3$ showing positive temperature coefficient of resistance. J. Appl. Phys. **66**, 3850-3856 (1989).

3 De Souza, R. A. & Chater, R. J. Oxygen exchange and diffusion measurements: The importance of extracting the correct initial and boundary conditions. Solid State Ionics **176**, 1915-1920 (2005).

4 De Souza, R. A. & Martin, M. Probing diffusion kinetics with Secondary Ion Mass Spectrometry. MRS Bull. **34**, 907-914 (2009).

5 Kilner, J. A., Skinner, S. J. & Brongersma, H. H. The isotope exchange depth profiling (IEDP) technique using SIMS and LEIS. J. Solid State Electrochem. **15**, 861-876 (2011).

6 Kofstad, P. K. Nonstoichiometry, diffusion and electrical conductivity in binary metal oxides. (John Wiley & Sons Inc New York, 1972).

7 Smyth, D. M. The defect chemistry of metal oxides. (Oxford University Press, New York, 2000).

8 Hiruma, Y., Nagata, H. & Takenaka, T. Thermal depoling process and piezoelectric properties of bismuth sodium titanate ceramics. J. Appl. Phys. **105**, 084112 (2009).

9 Sung, Y. S. et al. Effects of Bi nonstoichiometry in $Bi_{(0.5+x)}Na_{0.5}TiO_3$ ceramics. Appl. Phys. Lett. **98**, 012902 (2011).

10 Rivera, A. et al. Percolation-limited ionic diffusion in $Li_{0.5-x}Na_xLa_{0.5}TiO_3$ perovskites ($0 <= x <= 0.5$). Chem. Mater. **14**, 5148-5152 (2002).

11 Geneste, G., Kiat, J.-M., Malibert, C. & Chaigneau, J. Experimental and first-principles study of the structure and dielectric response of the high-temperature quantum paraelectric $La_{1/2}Na_{1/2}TiO_3$. Phys. Rev. B **75** (2007).

12 Jones, G. O. & Thomas, P. A. Investigation of the structure and phase transitions in the novel A-site substituted distorted perovskite compound $Na_{0.5}Bi_{0.5}TiO_3$. Acta Crystallogr., Sect. B: Struct. Sci **58**, 168-178 (2002).

13 Gorfman, S. & Thomas, P. A. Evidence for a non-rhombohedral average structure in the lead-free piezoelectric material $Na_{0.5}Bi_{0.5}TiO_3$. J. Appl. Crystallogr. **43**, 1409-1414 (2010).

14 Aksel, E. et al. Monoclinic crystal structure of polycrystalline $Na_{0.5}Bi_{0.5}TiO_3$. Appl. Phys. Lett. **98**, 152901 (2011).

15 Aksel, E., Forrester, J. S., Kowalski, B., Jones, J. L. & Thomas, P. A. Phase transition sequence in sodium bismuth titanate observed using high-resolution x-ray diffraction. Appl. Phys. Lett. **99** (2011).

16 Levin, I. & Reaney, I. M. Nano- and mesoscale structure of $Na_{1/2}Bi_{1/2}TiO_3$: A TEM perspective. Adv. Funct. Mater. **22**, 3445-3452 (2012).

17 Dorcet, V. & Trolliard, G. A transmission electron microscopy study of the A-site disordered perovskite $Na_{0.5}Bi_{0.5}TiO_3$. Acta Mater. **56**, 1753-1761 (2008).

18 Dorcet, V., Trolliard, G. & Boullay, P. Reinvestigation of phase transitions in $Na_{0.5}Bi_{0.5}TiO_3$ by TEM. Part I: First order rhombohedral to orthorhombic phase transition. Chem. Mater. **20**, 5061-5073 (2008).

19 Trolliard, G. & Dorcet, V. Reinvestigation of phase transitions in $Na_{0.5}Bi_{0.5}TiO_3$ by TEM. Part II: Second order orthorhombic to tetragonal phase transition. Chem. Mater. **20**, 5074-5082 (2008).

20 Groeting, M., Hayn, S. & Albe, K. Chemical order and local structure of the lead-free relaxor ferroelectric $Na_{1/2}Bi_{1/2}TiO_3$. J. Solid State Chem. **184**, 2041-2046 (2011).

21 Keeble, D. S. et al. Bifurcated polarization rotation in bismuth-based piezoelectrics. Adv. Funct. Mater. **23**, 185-190 (2012).

22 Schütz, D. et al. Lone-pair-induced covalency as the cause of temperature- and field-induced instabilities in bismuth sodium titanate. Adv. Funct. Mater. **22**, 2285-2294 (2012).